Journal of Innovative Optical Health Sciences
Vol. 4, No. 1 (2011) 1–7

DOI: 10.1142/S1793545811001289

FRACTAL NATURE OF LIGHT SCATTERING IN TISSUES

STEVEN L. JACQUES
Dermatology and Biomedical Engineering
Oregon Health and Science University
3303 SW Bond Ave, Portland
OR, 97239, USA
jacquess@ohsu.edu

Light scattering by a tissue has a wavelength dependence that depends on the size distribution of scatterers in the tissue. By measuring the wavelength dependence of scattering, one can deduce changes in the nanoscale architecture of cells and tissues. This report discusses the connection between nanoscale architecture and measurable light scattering. The significance of this work is to develop label-free optical imaging that describes tissue structure, to complement the absorption, fluorescence, and Raman scattering spectra that describe the chemical constituents of a tissue.

Keywords: Optical scattering; fractal; biomedical optics.

1. Introduction

Optical scattering measurements offer a label-free means of characterizing cells and tissues. In other words, without requiring added dyes or chemical agents, optical scattering can provide information about the biomaterial. Hence, optical scattering is an especially attractive approach toward noninvasive *in vivo* imaging and spectroscopy of tissues in medicine and biology. This paper discusses the nature of light scattering in biomaterials, which is the basis for such noninvasive interrogation of tissues.

2. The Mechanism of Light Scattering

The scattering of light by cells and tissues involves the redirection of incident photons into a new direction. The electromagnetic field of the light induces dipoles in the molecules of the biomaterial, and the collapse of dipoles reradiates photons in an angular dipole pattern. If the density of molecules allowing inducible dipoles is uniform, there is no scatter because there is constructive interference of all the reradiated fields from all the dipoles in the original incident direction and destructive interference at all off-axis angles of reradiation. For example, clear glass does not scatter, although glass is very dense and presents many inducible dipoles, which is why the refractive index (n) of glass is high. Figure 1 illustrates schematically how a uniform distribution of dipoles does not scatter light, but a nonuniform distribution of dipoles does scatter light.

Biological tissue presents a hierarchy of structure extending from $\sim$10 nm membranes to $\sim$10 μm nuclei (Fig. 2). Larger structures such as cells (10–30 μm) and arrays of cells (100's μm) may also redirect light, although at some point as structures get larger, it is perhaps more appropriate to think of these structures as microlenses or microlens arrays.

Therefore, a discussion of light scattering by biological tissues becomes a discussion of size distribution in the nano-architecture and micro-architecture of cell interiors and extracellular structures (e.g., fibers, basement membranes). The term

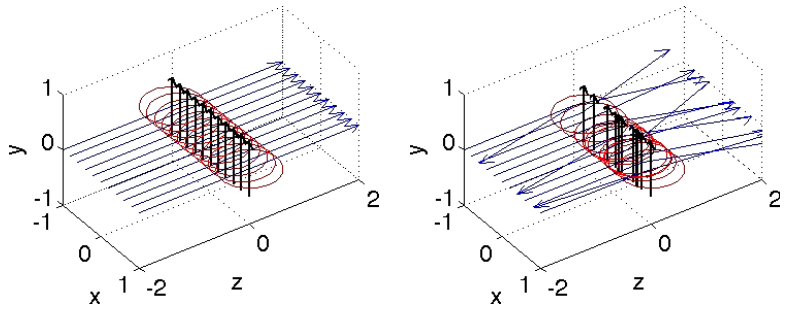

Fig. 1. Schematic depiction of scattering. (a) A uniform density of dipoles induced by an incident wave of light reradiates such that off-axis propagation destructively interferes and the transmitted light remains unscattered. (b) A nonuniform density of dipoles fails to destructively interfere off-axis propagation, and photons scatter.

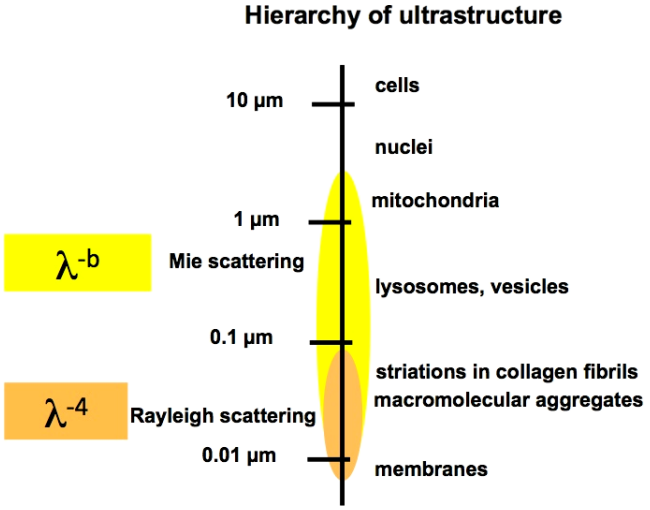

Fig. 2. Hierarchy of light-scattering structures in cells and tissues. Particles much smaller than the wavelength of light scatter proportional to λ^{-4} (Rayleigh scattering). Particles comparable to or greater than the wavelength of light scatter proportional to λ^{-b}, where $b \approx 1$ (Mie scattering).

"particle" is loosely used here to refer to structures that present variation in refractive index, which usually corresponds to variation in local mass density, such that a variation in inducible dipoles occurs, which scatters light. Such a "particle" can be a discrete structure, like a nucleus, or a continuum of density fluctuations, such as the variation in chromosome density within a nucleus.

3. A Fractal Size Distribution for Scattering Particles in a Tissue

The term "fractal" as applied to the size distribution of particles in cells and tissues implies that the relative ratio of larger to smaller particles is the same, regardless of the field of view, when using a microscope with different powers of magnification. This fractal relation can be simply described as a power law dependence to the size distribution:

$$\eta(d) = A\left(\frac{d}{1\,\mu m}\right)^{-B}, \tag{1}$$

where $\eta(d)$ is a probability density function for the size ($d[\mu m]$) of particles, and A is a normalization factor with units $[\mu m^{-1}]$ such that

$$\int_{d_{min}}^{d_{max}} \eta(d)\mathrm{d}d = 1, \tag{2}$$

where d_{min} to d_{max} is the range of particle sizes contributing to light scattering. The factor B specifies the shape of the distribution. The literature has discussed such fractal size distributions with respect to smoke particles and the ultrastructure of biological specimens.[1–5]

4. Estimating Tissue Optical Properties Using Mie Theory and a Fractal Size Distribution

The scattering of light by tissue is described by a scattering coefficient, $\mu_s[cm^{-1}]$ that describes the probability of scatter per unit length of photon travel, and by the anisotropy of scattering, g (dimensionless), which describes the average $\cos(\theta)$, where θ is the deflection angle of a scattering event. These are combined in the "reduced scattering coefficient", $\mu_s' = \mu_s(1-g)[cm^{-1}]$, which is the pertinent term for describing light transport when multiple scattering occurs.

The particle-size dependence of μ_s, g, and μ_s' are illustrated in Fig. 3 based on Mie theory for scattering by small spheres of diameter d. While spheres are not an accurate depiction of tissue ultrastructure, Mie theory provides an instructive example of the behavior of a class of particles. For sizes much smaller than the wavelength of light (vertical dashed line), the values of μ_s and μ_s' increase as d^3. For sizes much larger than the wavelength of light, the values of μ_s and μ_s' decrease as d^{-1}. Sizes close to the wavelength of light are in the transition between these extremes. Figure 3 illustrates the Mie scattering behavior for each particular size d at one wavelength, $\lambda = 500\,\text{nm}$.

Given the number density, $\rho[\#/\mu\text{m}^3]$, of a sphere of size $d[\mu\text{m}]$ in a medium containing spheres, one calculates the values of μ_s and g at one wavelength $\lambda[\mu\text{m}]$ using Mie theory:

$$[Q_s\, g] = \text{Mie}\left(\frac{n_{\text{par}}}{n'_{\text{med}}}, \frac{\pi d}{\lambda/n_{\text{med}}}\right), \tag{3a}$$

$$\mu_s = \rho Q_s \frac{\pi d^2}{4}, \tag{3b}$$

which yields μ_s in units of $[\mu\text{m}^{-1}]$, since d and λ are expressed in μm. To convert to cm^{-1}, multiply by $10^4[\text{cm}^{-1}/\mu\text{m}^{-1}]$. The values n_{par} and n_{med} indicate the refractive index of the sphere particle and the surrounding medium. The Mie calculation yields the efficiency of scattering Q_s, such that Q_s times the geometrical cross-sectional area of the sphere, $\pi d^2/4$, yields the scattering cross-section σ_s. Then $\mu_s = \rho\sigma_s$. The anisotropy of scattering, g, is also specified by the Mie calculation. This report uses the MATLAB versions of Mie theory prepared by Maetzler.[6]

Now consider a mixture of spheres of various sizes, specified by the size distribution $\eta(d)$ in Eq. (1). One must express the number density $\rho[\mu\text{m}^{-3}]$ as a function of particle size to yield a number density distribution $\rho'(d)$ $[\mu\text{m}^{-3}$ per $\mu\text{m}]$ or $[\mu\text{m}^{-4}]$. Assume that the volume fraction of spheres in the medium is f_v. Then the number density distribution $\rho'(d)[\mu\text{m}^{-4}]$ is calculated:

$$\rho'(d) = \frac{\eta}{V_{\text{norm}}}, \tag{4a}$$

where

$$V_{\text{norm}} = \int_{d_{\min}}^{d_{\max}} \frac{\eta(d)}{f_v} \frac{\pi d^3}{6}\,\text{d}d, \tag{4b}$$

such that

$$f_v = \int_{d_{\min}}^{d_{\max}} \rho'(d) \frac{\pi d^3}{6}\,\text{d}d. \tag{4c}$$

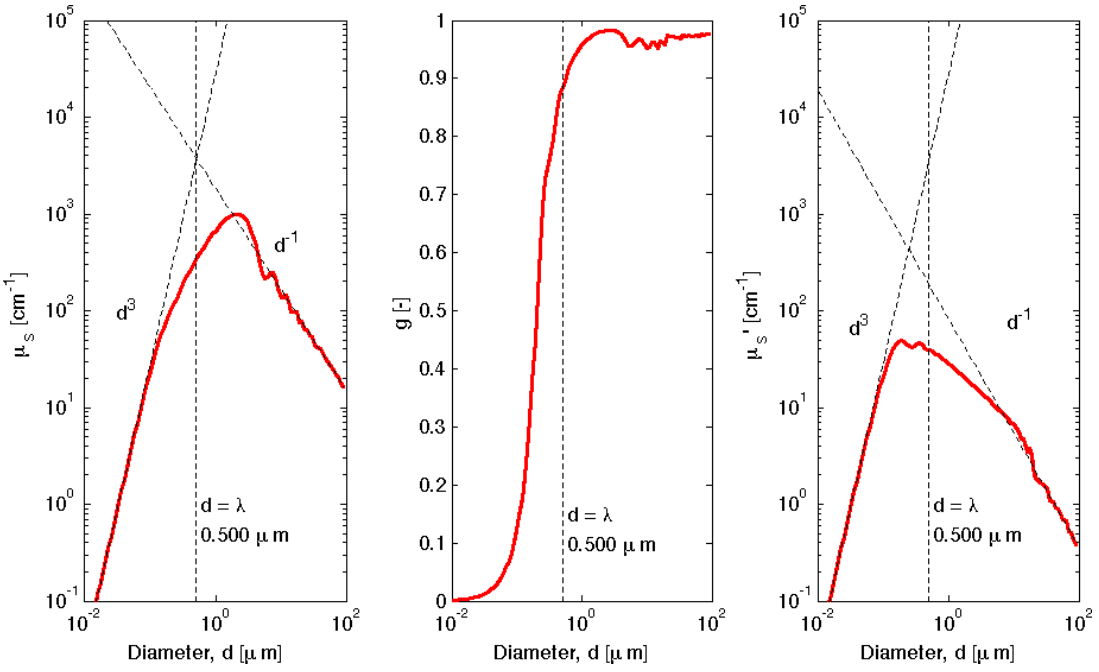

Fig. 3. The particle-size dependence of μ_s, g, and μ_s' for one wavelength, 500 nm for spherical particles ranging from $0.01-100\,\mu$m diameter d. The refractive indices of particle and medium are $n_{\text{par}} = 1.46$ and $n_{\text{med}} = 1.35$. The volume fraction of spheres is $f_v = 0.05$.

The factor $\pi d^3/6$ is the volume of a sphere of diameter d. The factor $V_{\rm norm}$ is a normalization constant with units of $[\mu{\rm m}^3]$ that serves to convert η into ρ' and to match the volume fraction f_v. Consequently, the density ρ equals $\rho' {\rm d}d$ for each particle size d.

Another factor must be considered, called the "packing factor", P [dimensionless]. This factor accounts for the decrease in effective scattering by particles due to their close packing which allows constructive interference to diminish the effectiveness of the particles in scattering light. This effect can be thought of as a decrease in the apparent $\rho'(d)$. P is a function of size d.

The $\rho'(d)$ and $P(d)$ can now be used to calculate the total values of μ_s and μ_s' for the mixture of spheres:

$$\mu_{s.{\rm total}} = \int_{d_{\rm min}}^{d_{\rm max}} \rho'(d) P(d) Q_s(d) \frac{\pi d^2}{4} {\rm d}d, \qquad (5a)$$

$$\mu'_{s\,{\rm total}} = \int_{d_{\rm min}}^{d_{\rm max}} \rho'(d) P(d) Q_s(d) \frac{\pi d^2}{4} (1 - g(d)) {\rm d}d, \qquad (5b)$$

and the total value of g for the mixture is calculated:

$$g_{\rm total} = 1 - \frac{\mu'_{s\,{\rm total}}}{\mu_{s.{\rm total}}}. \qquad (5c)$$

The wavelength dependence of μ_s' is experimentally observed to behave as

$$\mu_s'(\lambda) = a \left(\frac{\lambda}{1\,\mu{\rm m}} \right)^{-b}, \qquad (6)$$

and a similar expression can describe μ_s. Therefore, the functions $\mu_s'(\lambda)$ and $\mu_s(\lambda)$ can each be described by parameters a and b as in Eq. (6).

5. Example Calculation

To illustrate the calculation, and to illustrate the effect of the packing factor $P(d)$, the following example is considered. Consider a tissue with cells that contain a lipid content of 5% ($f_v = 0.05$) such that this lipid is organized into a hierarchy of structural aggregates approximated by spheres with diameter d ranging from $0.010 - 10\,\mu$m. The particle size distribution $\eta(d)$ is specified by Eq. (1) with $A = 2.69 \times 10^{-6} [\mu{\rm m}^{-1}]$ and $B = 4$. Let there be two types of packing factors: (a) $P(d)$ equal to a constant value of 1.00, (b) $P(d) = {\rm erfc}((0.0500\,\mu{\rm m}) - d)/(0.0500\,\mu{\rm m})/2$. These $\eta(d)$ and $P(d)$ are shown in Fig. 4.

Let the $n_{\rm par} = 1.46$ (lipid) and $n_{\rm med} = 1.35$ (aqueous solution with solutes $\approx$ cytoplasm). The estimated values of $\mu_{s.{\rm total}}$, $g_{\rm total}$ and $\mu'_{s\,{\rm total}}$ as functions of wavelength λ are calculated using Mie theory using Eqs. (3)–(5), and are shown in Fig. 5. A fit to the data using Eq. (6) is cited for μ_s and μ_s'. The solid red line and black dashed line show the results using the packing factor $P_{\#1}$ and $P_{\#2}$, respectively. The results specify optical properties that are in the approximate range observed for biological tissues.

The results illustrate a significant but modest effect of $P(d)$ on the optical properties. It should be noted that the $P_{\#2}$ used in this example is a rather strong packing factor affecting particles whose d match the wavelength of photons in the mid-visible spectrum. Moving $P(d)$ toward affecting smaller sizes causes the effect to lessen. More work on the nature of the packing factor must be done. It is possible that the peak magnitude of $P(d)$ may be less than one, thereby decreasing μ_s and μ_s'. It is interesting that $\mu'_{s\,{\rm total}}(\lambda)$ is more sensitive to $P(d)$ than $\mu_{s.{\rm total}}(\lambda)$, since $\mu'_{s\,{\rm total}}$ depends on both $\mu_{s.{\rm total}}$ and $g_{\rm total}$.

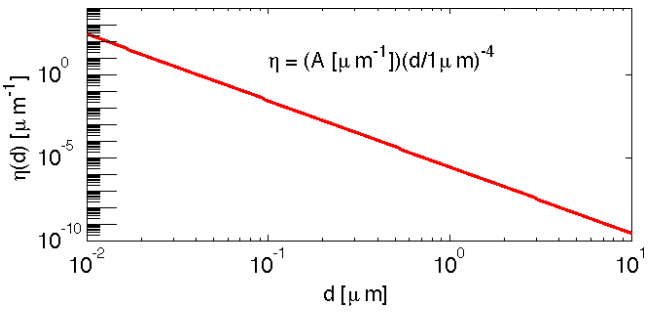

(a)

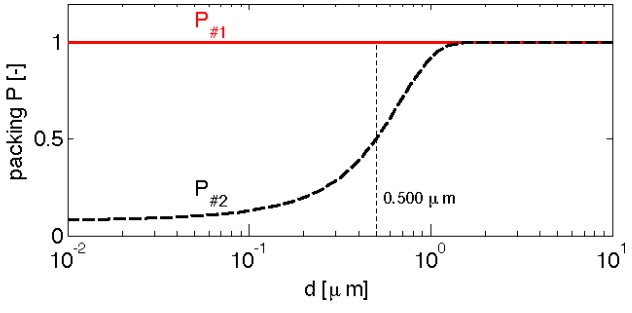

(b)

Fig. 4. (a) The particle size distribution $\eta(d)$. (b) The packing factor $P(d)$ as two curves, a constant $P_{\#1}$ and a $P_{\#2}$ that diminishes the contribution of particles smaller than 500 nm.

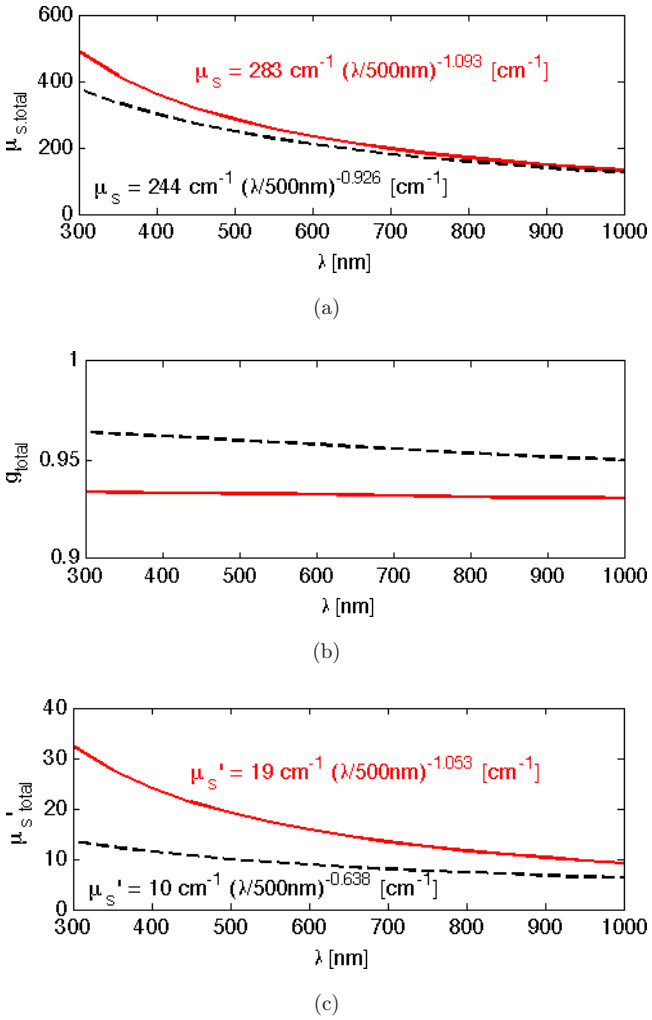

Fig. 5. (a) $\mu_{s.\text{total}}(\lambda)$; (b) $g_{\text{total}}(\lambda)$; (c) $\mu'_{s.\text{total}}(\lambda)$. The red solid line and black dashed line respectively show the results for the two packing factors, $P(d)$ equal to a constant $P_{\#1}$ or a varying $P_{\#2}$ that diminishes the contribution of particles smaller than 500 nm.

6. Add Extra Rayleigh Scattering if Collagen is Present

If there is a significant collagen content in the tissue, the behavior of scattering in tissues is not simply λ^{-b}, with $b \approx 1$. The fine structure of the collagen fibrils presents a large amount of Rayleigh scattering that behaves as approximately λ^{-4}. The total behavior of μ'_s can be described:

$$\mu'_s(\lambda) = a'\left(\frac{\lambda}{1\,\text{nm}}\right)^{-b_{\text{MIE}}} + c'\left(\frac{\lambda}{1\,\text{nm}}\right)^{-4} \approx a\left(\frac{\lambda}{1\,\text{nm}}\right)^{-b}. \quad (7)$$

For skin, $a' = 4.43 \times 10^3\,\text{cm}^{-1}$, $b_{\text{Mie}} \approx 0.91$, and $c' = 1.72 \times 10^{12}\,\text{cm}^{-1}$, such that μ'_s at 500 nm wavelength is $43\,\text{cm}^{-1}$. However, fitting the behavior in the limited spectral range of visible to near-infrared light with $a\lambda^{-b}$ yields $b \approx 2.3$. Figure 6 illustrates how fitting the limited range available from convenient measurements in the visible to near-IR can be reasonably approximated by $a\lambda^{-b}$, however, the projection of this scattering into the UV or mid-IR yields predictions that deviate from the expectations of Mie theory.

To connect this experimental behavior with the theoretical predictions of Mie theory, let us postulate two size distributions, $\eta_1 = A_1 d^{-8}$ for very small scatterers that only contribute Rayleigh scattering and yield $\sim\lambda^{-4}$ behavior (not shown), and $\eta_2 = A_2 d^{-4}$ which was shown in Sec. 4 to yield $\sim\lambda^{-1}$ behavior. The values of A_1 and A_2 properly normalize η_1 and η_2. Then we normalize each distribution so as to be consistent with the volume fraction f_v. Then we mix the two distributions by choosing a factor k_{Rayleigh} that specifies the amount of extra Rayleigh scattering to be included in the number density distribution:

$$\rho'(d) = k_{\text{Rayleigh}} \frac{\eta_1(d)}{\int_{d_{\min}}^{d_{\max}} \frac{\eta_1(d)}{f_v} \frac{\pi d^3}{6}\,\text{d}d} + (1 - k_{\text{Rayleigh}}) \frac{\eta_2(d)}{\int_{d_{\min}}^{d_{\max}} \frac{\eta_2(d)}{f_v} \frac{\pi d^3}{6}\,\text{d}d} \quad (8)$$

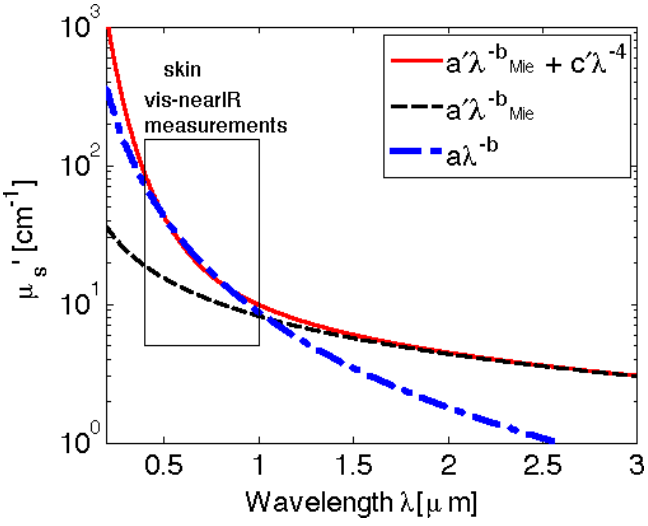

Fig. 6. The reduced scattering coefficient observed in the 400−1,000 nm visible to near-IR range experimentally behaves as the red solid line, $a'\lambda^{-b_{\text{Mie}}} + c'\lambda^{-4}$. The black dashed line is the Mie component $a'\lambda^{-b_{\text{Mie}}}$. The blue dash−dot line indicates the fit $a\,\lambda^{-b}$.

that is used in Eq. (5) to calculate $\mu_s'(\lambda)$. Then this $\mu_s'(\lambda)$ is fitted by $a\lambda^{-b}$ to yield a value b that characterizes the wavelength-dependent behavior of scattering.

Figure 7(a) shows the number density distribution $\rho'(d)$ as the value of k_{Rayleigh} is varied over several orders of magnitude. Figure 7(b) shows the value of b as the k_{Rayleigh} is varied, where the x-axis indicates $1-k_{\text{Rayleigh}}$ on a logarithmic scale. The case of $k_{\text{Rayleigh}}=1.0$ corresponds to the red line in Fig. 7(a) ($1-k_{\text{Rayleigh}}=0$), and the value of b in Fig. 7(b) is close to 4. The case of $k_{\text{Rayleigh}}=0$ corresponds to the blue line in Fig. 7(a) ($1-k_{\text{Rayleigh}}=1$), and the value of b in Fig. 7(b) is close to 1.

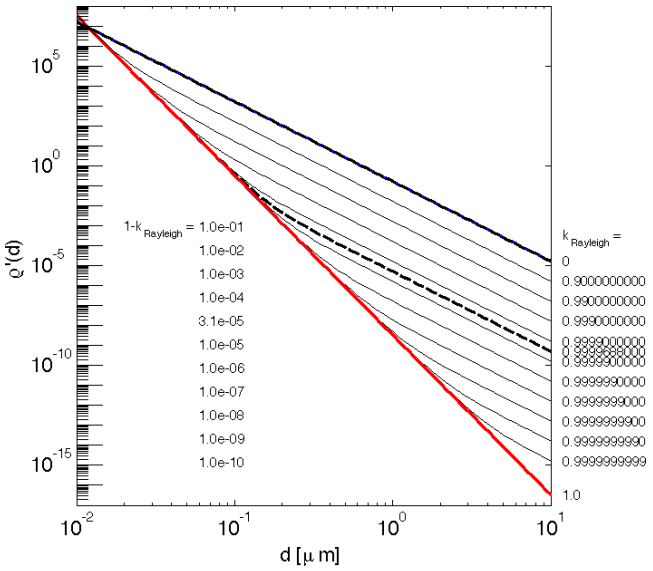

(a)

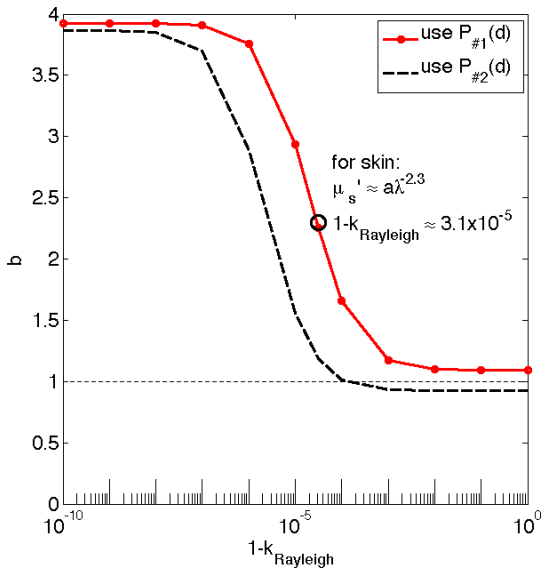

(b)

Fig. 7. (a) The number density distributions $\rho'(d)[\text{cm}^{-4}]$, as the fraction of pure Rayleigh scattering (k_{Rayleigh} in Eq. (8)) is varied. When $1-k_{\text{Rayleigh}}=10^{-5}, k_{\text{Rayleigh}}=0.999990$. Red line is $\rho'(d)$ for pure Rayleigh, $k_{\text{Rayleigh}}=1, \eta\approx d^{-8}$. The black line is for $k_{\text{Rayleigh}}=0, \eta\approx d^{-4}$. The dashed black line is the best estimate for the distribution of skin. (b) The factor b in the fit $\mu_s'(\lambda)=a\lambda^{-b}$. Skin behaves as $\lambda^{-2.3}$. The dashed black line indicates the calculation using the packing factor $P_{\#2}(d)$.

The best estimate for the $\rho'(d)$ that is appropriate for skin is shown as a dashed black line in Fig. 7(a), corresponding to $1-k_{\text{Rayleigh}}=3.1\times10^{-5}$, such that $\mu_s'(\lambda)\approx a\lambda^{-2.3}$.

The dashed black line in Fig. 7(b) indicates the calculation using the packing factor $P_{\#2}(d)$, which decreases the influence of Rayleigh scatterers, decreasing b for a particular k_{Rayleigh}. The packing factor becomes a strong effect when collagen presents a strong Rayleigh component to the scattering.

7. Discussion

The equations of Sec. 4 and the example of Sec. 5 outline how one can choose a fractal size distribution $\eta(d)=Ad^{-B}$, and predict the wavelength dependence of scattering, $a\lambda^{-b}$, for either μ_s or μ_s'.

The simple example of this paper illustrated the case of a cell composed of 5% lipid that was distributed as d^{-B} for $B=4$. The result is scattering that falls as λ^{-b} with $b\approx1$. However, if the packing factor strongly attenuates the contribution of smaller scale nano-architecture, the value of b drops. The example packing factor $P_{\#2}(d)$ in the example caused b to drop just a little to 0.925 for μ_s and to drop significantly to 0.639 for μ_s'. The $P_{\#2}(d)$ caused g to increase, and scattering became more forward-directed as the particle size distribution shifted to large particles. This observation suggests that the optical property μ_s' is more sensitive to the nano-architecture than μ_s, presumably because $\mu_s'=\mu_s(1-g)$ and g is sensitive to the size distribution.

Measurements sensitive to g should offer the best means of characterizing the nano-architecture of cells and tissues. In our laboratory, we have used reflectance-mode confocal microscopy and focus-tracked optical coherence tomography to specify the reflected light from the focus of an objective lens as the focus is scanned down into a tissue. The measurement yields an exponential,

$$R(z_{\text{focus}})=\rho e^{-\mu z_{\text{focus}}}, \tag{9}$$

which specifies the two parameters called reflectivity ρ [dimensionless] and attenuation $\mu[\mathrm{cm}^{-1}]$. These values map into the scattering coefficient μ_s and the anisotropy g (when the absorption coefficient μ_a is relatively low). Hence, the g of a tissue can be measured noninvasively. We have used this method to document the drop in g toward more isotropic scattering when skin has the mutation *osteogenesis imperfecta*, which interferes with proper assembly of collagen fiber bundles.[7] We have monitored the drop in g when metal−metalloproteinases degrade collagen in collagen gels.[8,9] We have monitored the increase in g when skin is soaked in glycerol to achieve optical clearing, apparently causing desiccation of the collagen.[10]

In summary, a Mie model for approximating tissue optical scattering as a mixture of nanoscale to microscale spheres of lipid in a medium containing solutes was outlined. The predictions yield values of scattering μ_s, anisotropy g, and reduced scattering μ_s' that are comparable to measured values in tissues.

References

1. C. M. Sorensen, J. Cai, N. Lu, *Appl. Opt.* **31**(30), 6547 (1992).
2. S. R. Forrest, T. A. Witten Jr., *J. Phys. A: Math. Gen.* **12**(5), L109 (1979).
3. J. M. Schmitt, G. Kumar, *Opt. Lett.* **21**(16), 1310 (1996).
4. C. M. Sorensen, *Aerosol Sci. Technol.* **35**(2), 648 (2001).
5. C. J. R. Sheppard, *Opt. Lett.* **32**(2), 142 (2007).
6. C. Mätzler, *Research Report No. 2002−08*, University of Bern, Institut für Angewandte Physik. (Download at http://omlc.ogi.edu/software/mie.)
7. R. Samatham, S. L. Jacques, P. Campagnola, *J. Biomed. Opt.* **13**(4), 041309 (2008).
8. D. Levitz, M. T. Hinds, N. Choudhury, N. T. Tran, S. R. Hanson, S. L. Jacques, *J. Biomed. Opt.* **15**(2), 026019 (2010).
9. D. Levitz, M. T. Hinds, A. Ardeshiri, S. R. Hanson, S. L. Jacques, *Biomaterials* **31**(32), 8210 (2010).
10. R. Samatham, K. G. Phillips, S. L. Jacques, *J. Innov. Opt. Health Sci.* **3**(3), 183 (2010).